Check for updates

Bi-doped BaBiO₃ (x = 0%, 5%, 10%, 15%, and 20%) perovskite oxides by a sol–gel method: comprehensive biological assessment and RhB photodegradation†

Wissam Bouchal,[a] Faiçal Djani,*[a] Djamel Eddine Mazouzi,[a] Rima Nour Elhouda Tiri,[bc] Soufiane Makhloufi,[a] Chaker Laiadi,[d] Arturo Martínez-Arias, [iD][e] Ayşenur Aygün[bc] and Fatih Sen [iD] *[bc]

The BaBiO₃ (BBO) perovskite oxide was prepared via a sol–gel method with different concentrations of Bi nitrate and examined as a photocatalyst for RhB degradation under sunlight, and its antioxidant and antibacterial activities were examined. X-ray diffraction (XRD) indicated the formation of a BaBiO₃–BaCO₃ (BBO–BCO) binary composite. For the degradation of RhB under solar radiation, high photocatalytic activity (73%) was observed. According to the antibacterial activity study, the addition of Bi enhanced the antibacterial activity of the resulting material against both Gram-positive and Gram-negative microorganisms. The Bi%–BBO (Bi 20%) inhibited 96.23% *S. aureus*. 10% Bi–BBO as an antioxidant agent had the most efficacious IC50 value of 2.50 mg mL⁻¹. These results seem to suggest that BBO–BCO is a promising catalytic material with potential application in the fields of catalysis and medicine.

1. Introduction

Nanotechnology has become one of the major fields of science and the sixth most innovative and promising technology, with significant influence on the international economy and society.[1–3] Nanomaterials are nanometre-sized particles (1 to 100 nm) that are frequently employed in nanoscience applications and research.[4,5] Due to their thermal conductivity, high surface-to-volume ratio, catalytic reactivity, and nonlinear optical performance,[6] these nanoparticles (NPs) are chemically stable. Nanotechnology is gaining importance owing to its various applications such as in electronics, information storage, optoelectronics,[7,8] chemical industries, environmental protection, drugs and pharmaceuticals, catalysis, antibacterial,[9] and antioxidants.[10] Due to the unique chemical, physical, and biological properties of NPs,[11] which include

their high catalytic activity, chemical stability, and antibacterial and antioxidant medicinal activities,[12,13] they have numerous and diverse applications. Materials nanoparticles such as CuO,[11] ZnO,[11,14,15] ZnFe₂O₄,[16] and LaNiO₃ (ref. 17) have been studied for environmental and biomedical applications. Alternatively, BaBiO₃, since it was first manufactured in 1993, has attracted continuous interest from scientists.[18] It is an oxide from the ABO₃ perovskites class, possessing interconnected BiO₆ octahedra[19] and a structured arrangement of bismuth ions. According to X-ray and neutron diffraction data,[20] the crystalline structure of the BaBiO₃ perovskite can be duplicated (Ba₂Bi³⁺Bi⁵⁺O₆), comprising of bismuth in two valence states, *i.e.*, Bi³⁺ and Bi⁵⁺.[21] Various groups have classified its symmetry as monoclinic, orthorhombic, rhombohedral, and triclinic. The BBO mixed oxide is a p-type semiconductor[22] with an extremely low bandgap (2 eV) and significant ability for absorbing visible light, resulting from the hybridized O 2p and Bi 6s orbitals in the valence bands (VBs), which reduce the bandgap.[23] BaBiO₃ particle samples have been synthesized using various techniques, including hydrothermal techniques,[24] sol–gel method,[25] and solid-state reactions.[26] It has been reported that the preparation method has subtle effects on the electronic structure, morphology, particle size, and light intensity of this compound.[27,28] The application of this ternary compound has been reported in various fields including superconductivity,[29] photovoltaics,[23] photoelectrochemical water splitting processes,[30] and photocatalysis.[31] Jain *et al.*[32] prepared BBO

ᵃMolecular Chemistry and Environment Laboratory, Mohammed KHIDER University Biskra, BP:145 RP, Biskra, 07000, Algeria. E-mail: f.djani@univ-biskra.dz

ᵇSen Research Group, Department of Biochemistry, University of Dumlupınar, 43000, Kütahya, Turkey. E-mail: fatihsen1980@gmail.com

ᶜSRG Incorporated Company, Kutahya Design & Technopole, Calca OSB Neighbourhood, 43100 Kutahya, Turkey

ᵈDepartment of Chemical Engineering, Mohammed KHIDER University, Biskra 07000, Algeria

ᵉInstituto de Catálisis y Petroleoquímica, CSIC, C/Marie Curie 2, Campus de Cantoblanco, 28049 Madrid, Spain

from barium and bismuth nitrates using the Pechini method and confirmed the formation of $BaBiO_3$ phase in a monoclinic structure and its band gap was calculated from UV-VIS DRS and found to be 2.07 eV. Subsequently, the prepared perovskite was used as a photocatalyst to degrade the drug ibuprofen under visible light. The removal rate was 60% after 180 min of irradiation. According to Tang and coworkers,[31] the BBO perovskite synthesized from $Ba(NO_3)_2$ and $Bi(NO_3)_3 \cdot 5H_2O$ showed photocatalytic properties for the degradation of acetaldehyde and methylene blue. The oxide crystallizes in a monoclinic structure, where the Bi^{3+} and Bi^{5+} ions coexist. The theoretical calculation indicated that this material has an indirect band gap (indirect semiconductor), and then the synthesized oxide can decompose methylene blue dye with a degradation rate of 75% after 120 min under Xe lamp irradiation. Sharma et al.[33] used $BaBiO_3$ synthesized via the Pechini route as a photocatalyst for the degradation of malachite green dye under visible light. The prepared oxide calcined at 800 °C had an optical band gap of 2.07 eV and showed a strong fundamental absorption edge at 600 nm. The decomposition of malachite green dye followed pseudo-first-order kinetics. This bismuthate was synthesized by Shilna et al.[19] via the sol–gel technique using barium nitrate $(Ba(NO_3)_2)$ and bismuth nitrate $(Bi(NO_3)_3 \cdot 5H_2O)$ dissolved in ethylene glycol and they performed magnetic and resistivity measurements, indicating the presence of ferromagnetic domains. The research by Gao et al.[34] revealed that the structural monoclinic $BaBiO_3$ phase had optical band gaps between 2.07 and 1.81 eV. They also used DFT to perform first-principles calculations and discovered that $BaBiO_3$ is predicted to be a promising p-type conductive oxide due to its excellent electrical conductivity (0.16 S cm^{-1}) and light hole effective mass (0.445 m_0 and 0.563 m_0). The photocatalytic reduction of CO_2 to methane and CO under visible light was investigated by Khraisheh et al.[35] in the presence of $BaBiO_3$ prepared via solid-phase synthesis and calcined at high temperature using Bi_2O_3 and $BaCO_3$ as precursors, which had an absorption band edge of 2.04 eV. Based on previous studies, we determined that the above-mentioned oxide has been used in several applications and yielded highly effective results. However, it has never been used in the biological field as an antioxidant or antibacterial. $BaBiO_3$ nanoscale powder was synthesized via the sol–gel method to investigate its catalytic activity for the degradation of Rhodamine B dye, one of the most difficult to degrade and dangerous colorants, under sunlight, and then the possibility of its reuse for multiple cycles studied. Rhodamine B, which is classified as a water-soluble cationic pigment, can cause many harmful effects such as cancer, respiratory infections, and skin problems. However, due to its stability and difficulty in degradation, its removal remains a challenge and there is a need to find an effective, economical, and environmentally friendly ways to achieve this. In addition, to examine the antioxidant activity of the prepared powder using the DPPH reduction technique and its antibacterial activity for two types of bacteria, i.e., E. coli and S. aureus, while considering the enhancement in both its physicochemical and catalytic properties, an excess of bi-

nitrate was added to determine its effect on the studied properties.

2. Materials and methods

2.1. Synthesis of $BaBiO_3$ and Bi excess

To study the effect of excess Bi on the structure of the $BaBiO_3$ (BBO) perovskite, via the sol–gel method: 1 mol of $Ba(NO_3)_2$ (from Panreac), 1 mol of $Bi(NO_3)_3 \cdot 5H_2O$ (from Biochem), an excess of 5–10–15 and 20% of the mass of $Bi(NO_3)_3 \cdot 5H_2O$ were dissolved in distilled water, and then mixed with 2 mol of citric acid under heating at 80 °C for 12 h until a white gel was obtained. Subsequently, this gel was placed in an oven overnight to dry. After grinding the dried powder, TG analysis was carried out to determine the calcination temperature. Finally, the resulting powder was treated thermally at 900 °C for 8 h at a rate of 5 °C min^{-1}.

2.2. Characterization of $BaBiO_3$ and Bi excess

The thermal decomposition of the precursors (prior to calcination) was investigated by thermogravimetric analysis (TGA) using a METTLER TOLEDO TGA/DSC 3+ instrument from 25 °C to 1000 °C, at a heating rate of 10 °C min^{-1} in an air atmosphere. The crystallographic information of the powder samples was obtained via powder X-ray diffraction (Bruker AXS D8 Advance) employing Cu-K_α radiation ($\lambda = 1.542$ Å) in the 2θ range of 5° to 90°. The crystalline phases were identified by comparing them to the JCDDS standard using the X'pert High Score program. Fourier transform infrared spectroscopy was performed using a PerkinElmer VATR 2 spectrophotometer in ATR-FTIR mode to investigate the characteristic peaks of the as-synthesized powders in the spectral range of 2000–400 cm^{-1}. The UV-VIS diffuse reflectance spectra of the synthesized samples were acquired using a Cary 60 UV-VIS spectrophotometer and the band gap E_g was determined using the obtained data. The surface morphology was examined using a Quanta SEM Prisma E de Thermo Scientific scanning electron microscope. The SEM was equipped with an energy-dispersive X-ray analyser (EDX), which was used to determine the elemental composition. The specific surface area (S_{BET}) was obtained by applying the BET method to the nitrogen adsorption/desorption isotherm acquired at −196 °C with a Micrometrics ASAP 2020 Plus 2.00. All the samples were degassed overnight at 150 °C before adsorption. The Barrett–Joyner–Halenda (BJH) approach was used to determine the pore size distribution (pore diameter and sample volume).

2.3. Determination of photocatalytic activity

The photocatalytic activity of the synthesized oxide was evaluated using Rhodamine B as the pollutant under sunlight irradiation. Before performing the various analyses, the decomposition of RhB was performed in the absence of photocatalyst with and without light for 24 h. No change in the absorbance of RhB was detected in these blank experiments. For this test, 250 mL of RhB solution (2.087×10^{-4} M) and 1 mg mL^{-1} of the oxide were placed in the dark for 30 min with agitation to ensure adsorption/desorption equilibrium. Subsequently, the solution was exposed to sunlight
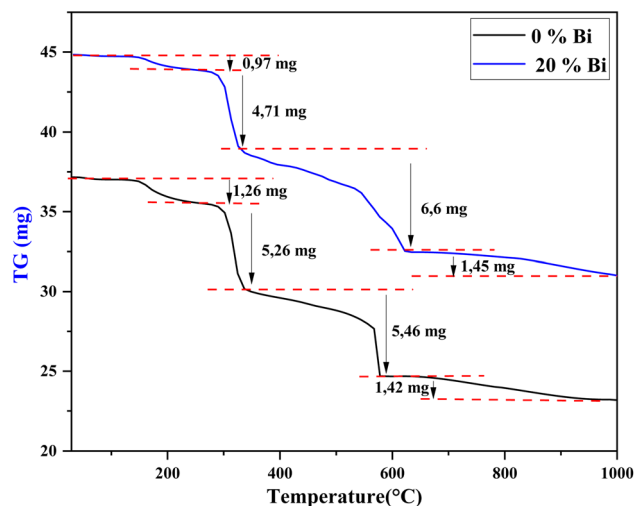
Fig. 1 TG curves of $BaBiO_3$–$BaCO_3$ (pure – 20% Bi) precursors heated in air at 5° min^{-1}.

for 210 min, and the agitation process was maintained to preserve the homogeneity of the mixture. A specimen was withdrawn at 30 min intervals, followed by centrifugation for removing the NPs. The absorbance of the solution containing the supernatant was measured using a Uviline 9400 spectrophotometer. The photo-degradation rate was calculated using the following equation:

$$\% \text{ of degradation} = \frac{C_0 - C_t}{C_0} \times 100$$

where C_0 and C_t are the initial and the measured concentration of RhB in the solution, respectively, at $\lambda_{max} = 554$ nm. The recycling studies were successfully carried out to study the recyclable properties of the BBO photocatalyst. Following each photocatalytic reaction, the BBO photocatalyst was centrifuged and rinsed with distilled water, followed by ethanol and acetone, and then dried at 60 °C for reuse.

2.4. Determination of antioxidant activity

The antioxidant power of BBO was evaluated *via* the DPPH (1,1-diphenyl-2-picrylhydrazyl) method, as described by Jaidee *et al.*[36] Different concentrations of BBO powder (1, 2, 3, 4, and 5 mg mL^{-1}) were incorporated in 1 mL of ethanoic DPPH solution and left in the dark for 30 min. The formula used to determine the percentage of inhibition:

$$IP = \frac{A_0 - A_t}{A_0} \times 100$$

where A_0 and A_t are the absorbance of the control and test sample, respectively, at $\lambda_{max} = 517$ nm. A linear regression analysis was performed to determine the IC50 value for the sample. Subsequently, the obtained results were compared with that of ascorbic acid (1, 2, 3, 4, and 5 mg).

2.5. Antibacterial activity

The antibacterial properties of BBO against *E. coli* and *S. aureus*, two harmful bacteria to humans, were evaluated with

a variation in excess Bi (%). A loop was used to transport the bacteria from the stock bacterial culture to a liquid medium, where they were cultured for 24 h. The absorbance values of the bacterial cultures were measured after 24 h and a 0.5 McFarland concentration of bacterial culture was added to the culture created for the antibacterial test trials of the catalyst in accordance with the reference procedure.[37] The necessary calculations were done for the excess (%) Bi concentration tests at several levels (0%, 5%, 10%, 15%, 20%). The antimicrobial tests were performed using 96-well plates. The bacterial culture containing the catalyst was cultivated for 24 h in a shaker in an incubator at 37 °C to track the growth of the bacteria and effects of the nanoparticles. After 24 h, the absorbance values at 600 nm of the bacterial culture were measured using a spectrophotometer. The percentage of bacterial inhibition of the bacterial cells at various Bi (%)–BBO concentrations was assessed using the absorbance readings.

3. Results and discussion

3.1. Characterization

3.1.1 Thermogravimetric analysis. A thermogravimetric analysis was performed to estimate the calcination temperature required for obtaining the BBO oxide. The TGA thermograms of the two precursors, *i.e.*, pure BBO and 20% Bi–BBO, as shown in Fig. 1, reveal four mass losses during heating from RT to 1000 °C in the range of 30–240 °C, 240–330 °C, 330–625 °C, and 625–1000 °C, with a total weight loss of 37.5% (14.40 mg) and 30.6% (13.73 mg) for the pure BBO and 20% Bi–BBO, respectively.

The first mass loss from 30 °C to 240 °C can be attributed to the evaporation of residual water and organic compounds
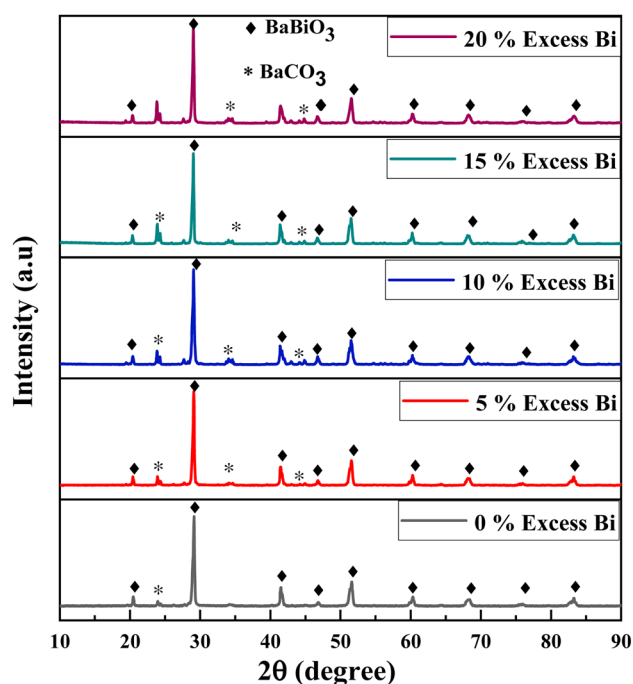

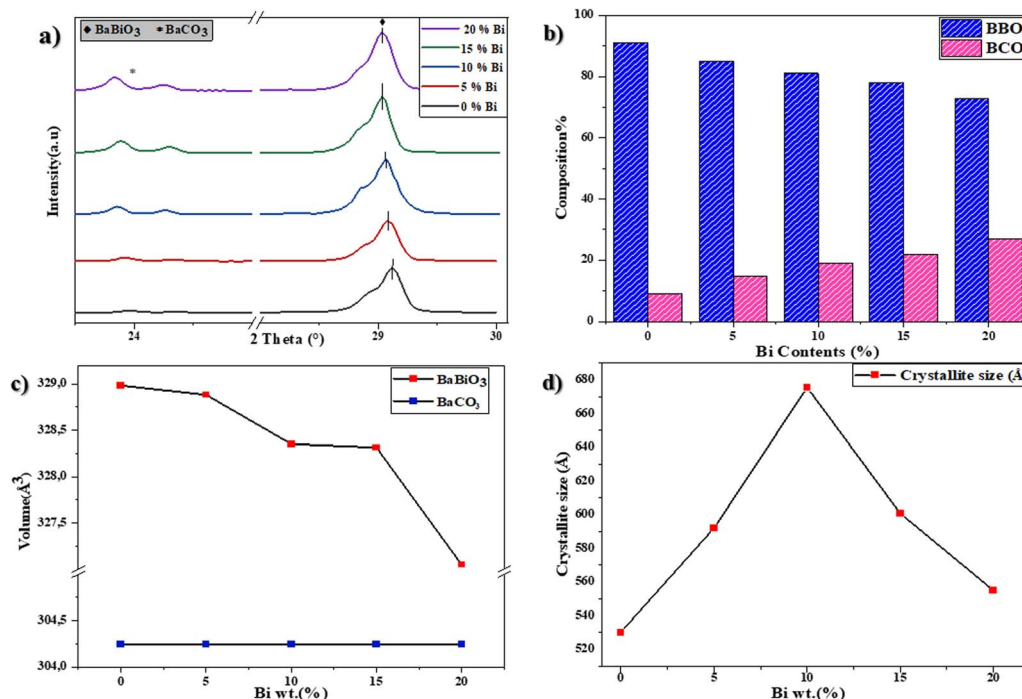**Fig. 2** XRD patterns of the BBO–BCO powders with different excess of Bi.

Fig. 3 (a) Evaluation of the highest X-ray diffraction peak positions for BBO and BCO, (b) BCO and BBO composition as a function of Bi content (%), (c) dependence of lattice volume on bismuth content for BBO and BCO and (d) plot showing the evaluation of average crystallite size of Bi%−BBO with Bi wt. (%).
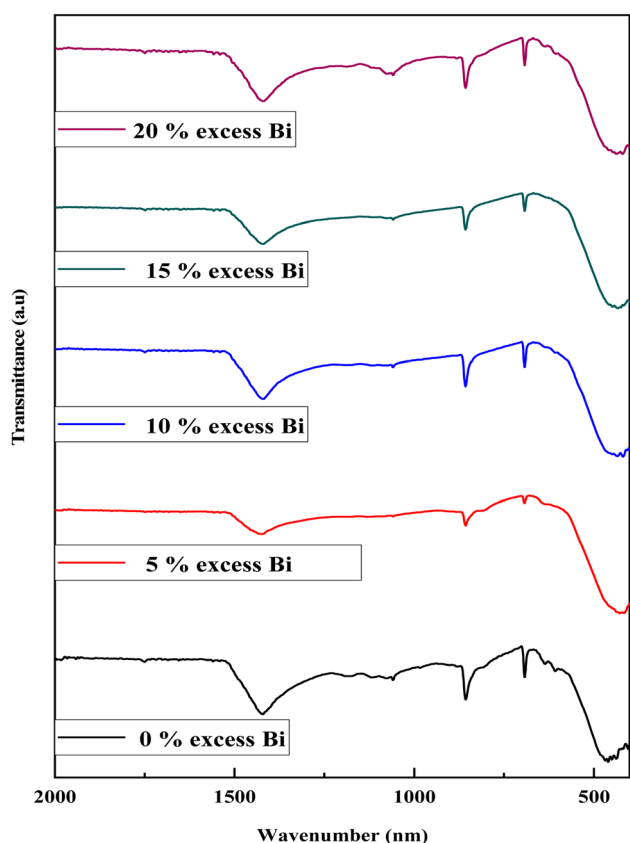

Fig. 4 FTIR spectra of % Bi−BBO powder samples calcined at 900 °C.

(partial decomposition of the citric acid molecule).[37] The second loss of mass between 240 °C and 330 °C corresponds to the pyrolysis and combustion of organic substances[33] and the formation of $BaCO_3$. The third mass loss between 330 °C and 625 °C is attributed to nitrate combustion (decomposition). The last mass loss detected from 625 °C to 1000 °C is relatively small and attributed to the formation of the perovskite structure. Accordingly, it was concluded that 900 °C is the optimal calcination temperature for achieving the intended phase.

3.1.2 X-ray diffraction analysis. The diffractograms of the powder calcined at 900 °C with different Bi excess are shown in the Fig. 2. The phase identification of the samples indicates that they correspond mainly to the perovskite structure (barium bismuthate) with a monoclinic structure (ICSD file 98-017-2757) and the presence of a minor $BaCO_3$ secondary phase (orthorhombic structure)[38] according to ICDD file 00-005-0378, implying the formation of the $BaBiO_3$–$BaCO_3$ binary composite system.

The diffraction peaks for the $BaBiO_3$ system appear at the most intense 2θ diffraction angles (20.375°; 29.019°; 41.439°; and 51.174°), and peaks at 2θ angles corresponding to the $BaCO_3$ system phase (23.9°; 34.087°; and 41.986°), with the Miller indices (hkl) of $BaBiO_3$ and $BaCO_3$ of (11−1) (111), (22−2), and (11−3), and (111), (112), and (221), respectively. The cell parameters of the binary composite formed were calculated for all the values of excess Bi from diffractograms with Rietveld refinement. All the structural parameters, including volume
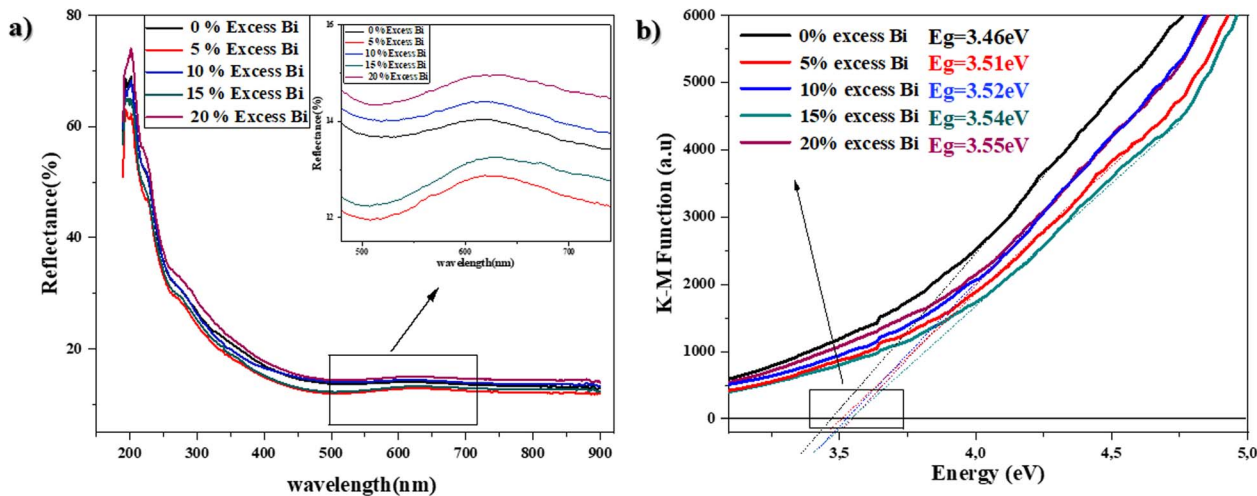
Fig. 5 (a) UV-Visible reflectance spectra and (b) graph used for band gap estimation of Bi%–BBO.

and crystalline size, are summarized in Table S1.† The crystallite size was calculated using the Scherrer equation,[39] as follows:

$$D = \frac{0.89\lambda}{\beta \cos\theta}$$

As shown in Fig. 3a, a gradual shift was observed in the main peak at 29.01° (111) for the BaBiO₃ majority phase towards lower angles with an increase in Bi concentration, which is in contrast with the difference in rays between the Ba^{2+} ionic ray greater than the Bi^{3+} ionic ray and can be explained based on the cation valence states.[40] Substitution at the A site of a valence Bi^{3+} ion for a Ba site causes a charge compensation transition from Bi^{3+} to Bi^{5+}, shifting the peaks towards lower angles. The intensity of the main peak (most intense peak) 23.9° Miller index (111) of the $BaCO_3$ minority phase, increased with an increase the Bi content and is related to the percentage of the $BaCO_3$ formed (0% Bi: 9%, 5% Bi: 15%, 10% Bi: 19%, 15% Bi: 22%, and 20% Bi: 27%).

Fig. 3b shows the evolution of $BaCO_3$ formation as a function of the Bi content added with the precursors. The percentage of $BaCO_3$ formed with 0% Bi added to BaBiO₃ (0% Bi–BBO) is 9%, and with an increase in the latter (20% Bi–BBO), 27% $BaCO_3$ formed with 73% BaBiO₃, indicating that Ba is substituted by the added excess Bi. Subsequently, the substituted Ba^{2+} ions are combined with the CO_3^{2-} ions from the complexing agent (citric acid) to form $BaCO_3$. The cell volume of BaBiO₃ decreased

with an increase in the Bi content in the samples. This decrease can be explained by the fact that the larger Ba^{2+} ions are replaced by the smaller Bi^{3+} ions in the perovskite A site (the atomic radius of Ba is larger than that of Bi). Alternatively, the volume of the $BaCO_3$ lattice remains constant with all percentages of Bi excess given that the lattice did not undergo any substitution (Fig. 3c). As can be seen in Fig. 3d, the average crystallite size (ACS) of Bi%–BBO varied between 51 and 67 nm. It can be observed that as the Bi% content increased from 0 to 10%, the average crystallite size of the particles increased, while with a further increase in the Bi content to 15% and 20%, the ACS of the binary composite decreased gradually. The minimum crystalline size was observed for pure BBO (51 nm).

3.1.3 IR spectroscopy analysis. To study the main functional groups of the synthesized products, FTIR spectroscopy in ATR mode was carried out, and the spectra were recorded between 2000 and 400 cm⁻¹ in transmission mode (Fig. 4).

The bands at around 1420 cm⁻¹ of the C–O bond of the carbonates[41] found in the $BaCO_3$ structure were confirmed by XRD, while the characteristic bands at around 850 cm⁻¹ in the five spectra are attributed to the deformation vibration of the BO_6 octahedra (Bi–O–Bi) and that of the Bi–O bond tetrahedral elongation vibrations are found at around 450 cm⁻¹.[42] The Ba–O band is present at around 690 cm⁻¹.

3.1.4 Diffuse reflectance spectroscopy analysis. UV-visible DRS spectrophotometry was carried out to measure the optical properties of the prepared % Bi–BaBiO₃ samples, where the

Table 1 Morphologic and optical parameters

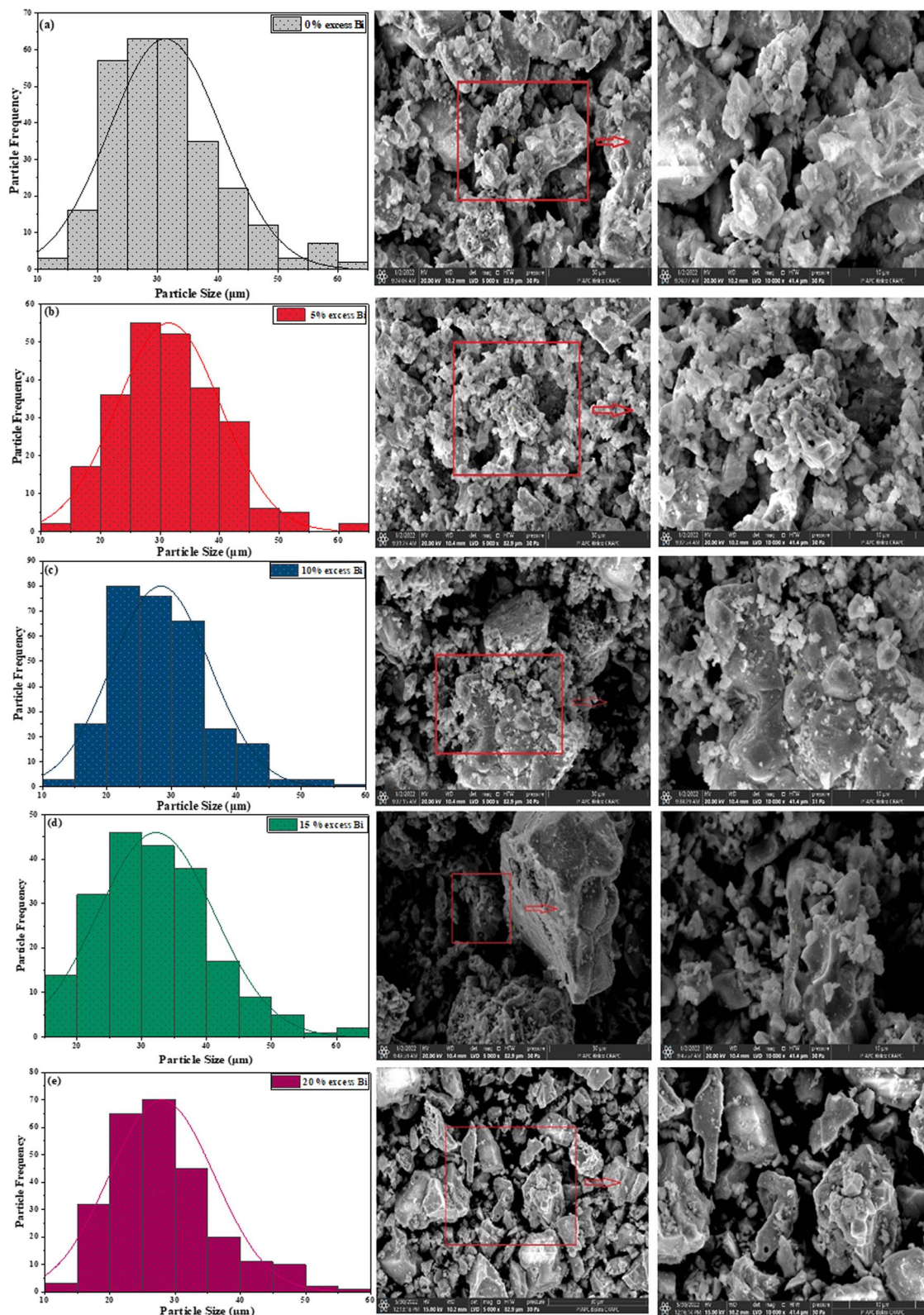| Oxide	Particle size (μm)	Band gap (eV)	BET (g m⁻²)	Average pore diameter (nm)	Average particle size (nm)
Pure BBO	26.18	3.46	0.1108	1.8213	6.84
5% Bi–BBO	27.05	3.51	0.8047	0.3643	5.16
10% excess of Bi	29.15	3.52	0.8770	0.8269	7.45
15% excess of Bi	30.61	3.54	1.2314	1.6807	4.87
20% excess of Bi	30.81	3.55	1.2853	1.8067	4.66

Fig. 6 Micrographs and particle size histograms for $BaBiO_3$–$BaCO_3$: (a) pure BBO, (b) 5% excess Bi, (c) 10% excess Bi, (d) 15% excess Bi, and (e) 20% excess Bi particles.
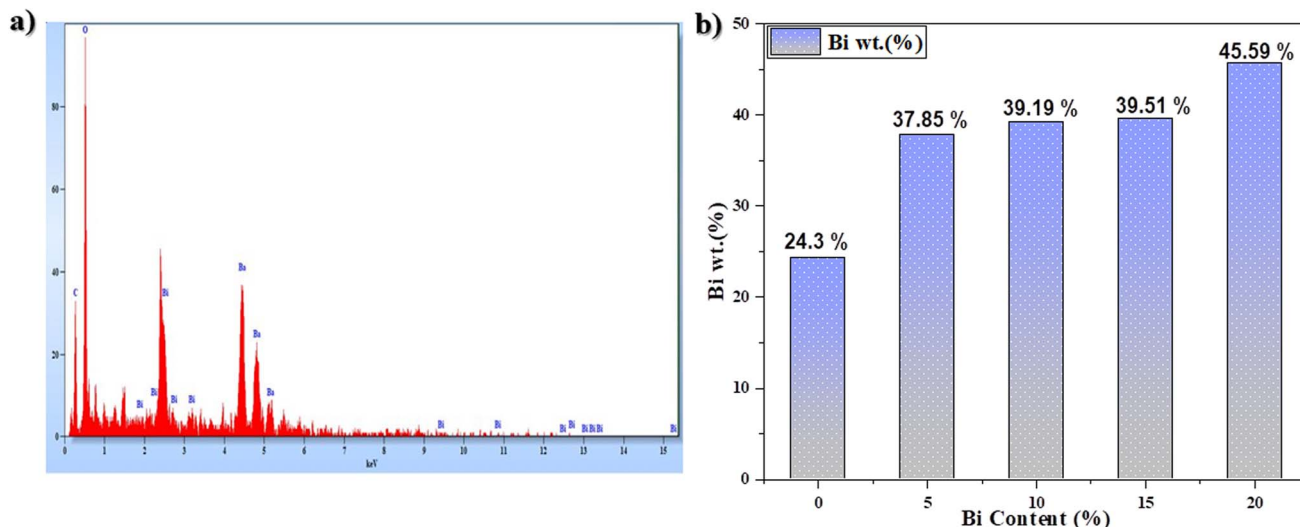
Fig. 7 (a) EDS spectrum of the as-prepared sample (20% excess Bi) and (b) variation in Bi wt% as a function of Bi content.

Table 2 EDS weight ratio of $BaBiO_3$–$BaCO_3$ with different excess of Bi NPs

	Weight (%)		
	Ba	Bi	O
Pure BBO	59.25	24.3	16.45
5% excess Bi	48.36	37.85	13.79
10% excess Bi	55.52	39.19	5.29
15% excess Bi	50.96	39.51	9.53
20% excess Bi	12.97	45.59	41.16

reflectance spectra were obtained from a scan in the 200–800 nm range, as shown in Fig. 5a.

Two bands, one at 200 nm and another smaller one at around 600 nm, were observed for all the BBO samples, indicating the photocatalytic activity of the prepared powder in visible light.[33] The optical gap of the powders was determined using the Kubelka–Munk function. The band gap value was obtained by extrapolating the linear part of the related plot of $(\alpha h\nu)^2$ vs. $h\nu$ up to $(\alpha h\nu)^2 = 0$.[31] The band gap energies (E_g) of the samples obtained at 900 °C are presented in Table 1. The E_g is between 3.55 and 3.46 eV (Fig. 5b), which is different from the previously reported values in the range of 1.81 eV to 2.25 eV in ref. 23 and 19. These high values can be explained by the presence of $BaCO_3$ with a gap of 5.51 eV.[43] These results show that the optical gap increased with the addition of Bi.

3.1.5 Scanning electron microscopy analysis. Scanning electron microscopy can be employed to obtain information about particle morphology, surface agglomeration, and grain size. The SEM micrographs of the samples synthesized and calcined at 900 °C (Fig. 6) showed an agglomerated structure (which can be due to the method of synthesis (sol–gel method) with uniform particle shapes). Heterogeneous surfaces were observed with a large grain size, which may be due to the presence of Bi in the samples.[44] This was confirmed by

calculating particle size using the ImageJ software and analysing 235 particles (Table 1). According to the values, the particle size of the samples increased from 26.18 to 30.81 μm with an increase in Bi content (0% Bi–BBO to 20% Bi–BBO, respectively).

More than SEM, EDS was used to validate the information provided by SEM. As is clear from Fig. 7a, Ba, Bi, and O appeared in the EDS spectrum and the abundance of the elements in the composition of the synthesized composites was measured in weight percent. Fig. 7b and Table 2 show an increase in the Bi abundance percentage with an increase in Bi content.

3.1.6 BET analysis. The specific surface area and pore size as a function of added Bi content obtained by the BET method are reported in Table 1. The specific surface area of the pure $BaBiO_3$ prepared sample is 0.1108 m^2 g^{-1}, which is somewhat slightly less than the value of 0.472 m^2 g^{-1} reported by Shtarev et al.,[45] who synthesized $BaBiO_3$ via the ceramic method, but still an order of magnitude higher than that of 0.047 m^2 g^{-1} reported by Khraisheh et al.,[35] who used the conventional solid-state reaction method. This specific surface area value increased with an increase in the excess Bi from 0% Bi–BBO to 20% Bi–BBO (0.1108, 0.8047, 0.8770, 1.2314 and 1.2853 m^2 g^{-1}, respectively). This growth is probably due to the existence of $BaCO_3$ with a high specific surface area of $S_{bet} = 27$ m^2 g^{-1}, as reported by Lee et al.[46] and 20.5 m^2 g^{-1} reported by Strobel et al.[47] Pore sizes ranging from 0.3643 to 1.8213 nm show that the binary composite $BaBiO_3$–$BaCO_3$ is a microporous material (<2 nm).[48]

3.2. Photocatalytic activity of Bi%–BBO

The photocatalytic activity of synthesized BBO was determined by examining its ability to degrade Rhodamine B under the influence of solar energy. The absorbance spectra of RhB in the present of BBO powder at various periods over 210 min are shown in Fig. 8, where the intensity of the characteristic peak at 554 nm decreased as a function of time.
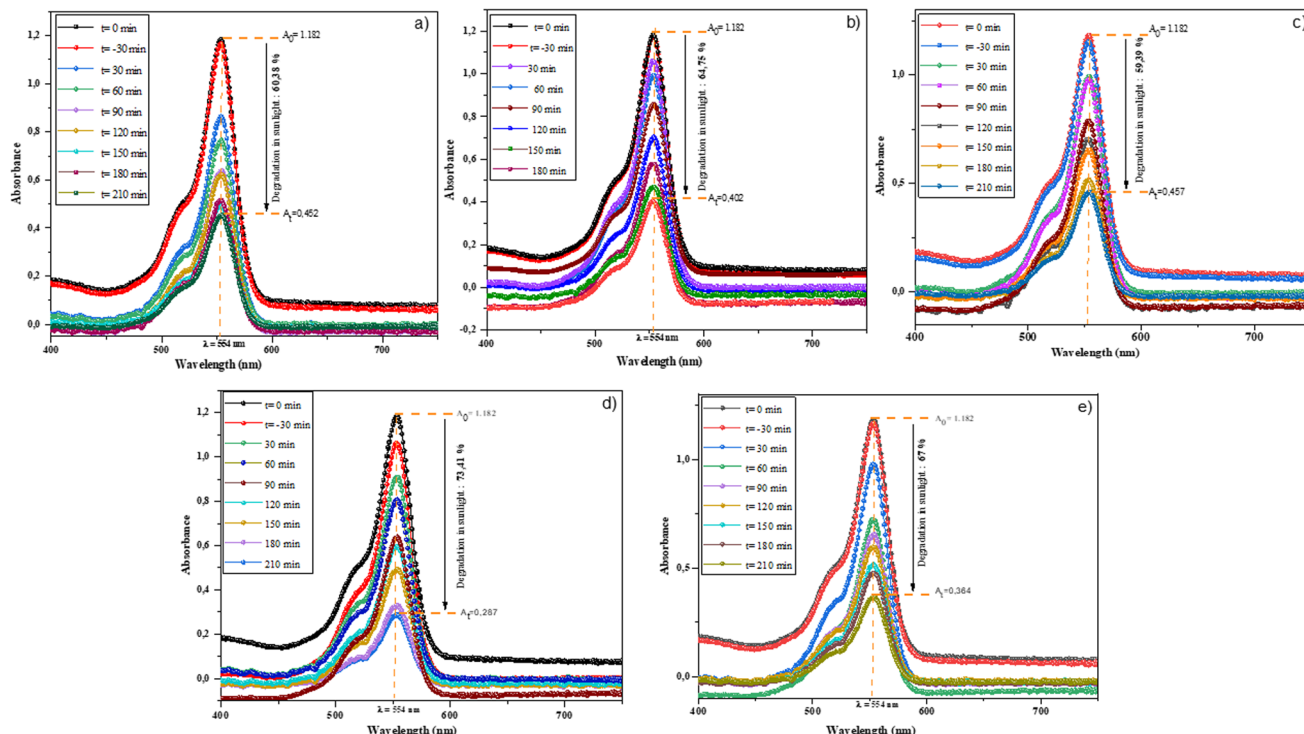
Fig. 8 Absorption spectra of RhB by BBO−BCO NPs under solar energy for different durations: (a) 0% Bi−BBO, (b) 5% Bi−BBO, (c) 10% Bi−BBO, (d) 15% Bi−BBO, and (e) 20% Bi−BBO.

The rate of RhB degradation for the samples of % Bi−BBO was between 59% and 73%, where 15% Bi−BBO exhibited the highest photodegradation compared to 10% Bi−BBO (Fig. 9a). It is clear that the crystallite size had no impact on the degradation efficiency. The unpredictable conduct in the consistent pace of photocatalytic decay with the progressive Bi surplus can be ascribed to the complex interplay in the electronic structure of the catalyst. This deviation may originate from non-monoclinic alterations in the dynamics of the charge carriers, surface reactivity, or recombination rates introduced by Bi, consequently impacting the general kinetics of decay.

The kinetic investigation offers substantial proof for comprehending the mechanism of degradation through photocatalysis. This is achieved by the estimation of the rate constant (k). There several models for studying the kinetics of the photodegradation reaction, including the Langmuir, Freundlich, Temkin, pseudo-first-order (PFO) and pseudo-second-order (PSO) models.[49−51] In this work, a kinetic study of the performance of the % Bi−BBO nanoparticles (NPs) in degrading RhB
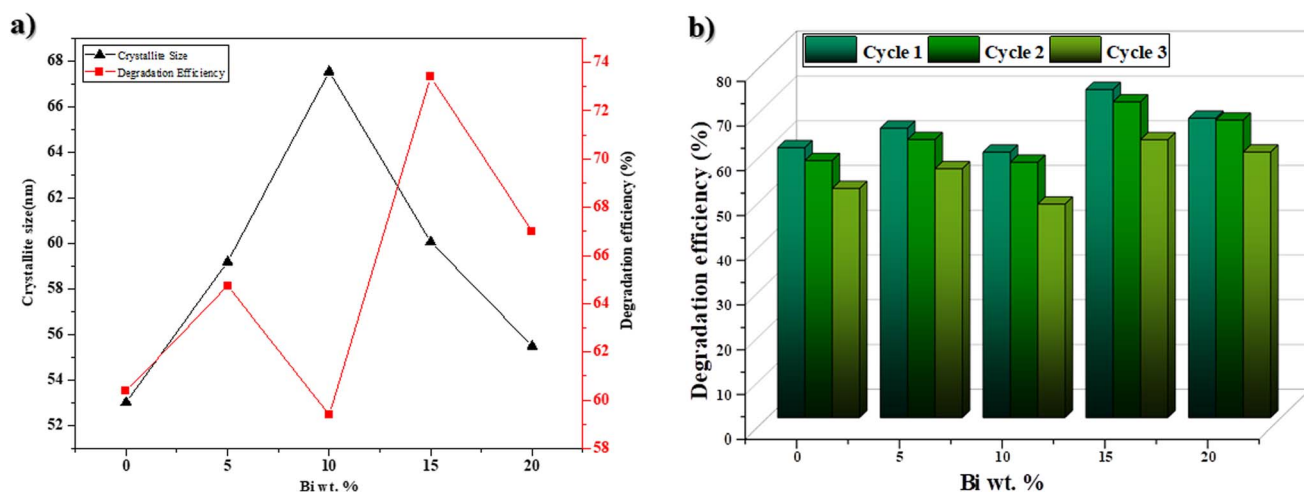

Fig. 9 (a) Relationship between degradation efficiency and crystallite size and (b) recycling of Bi%−BBO for the photodegradation of RhB.
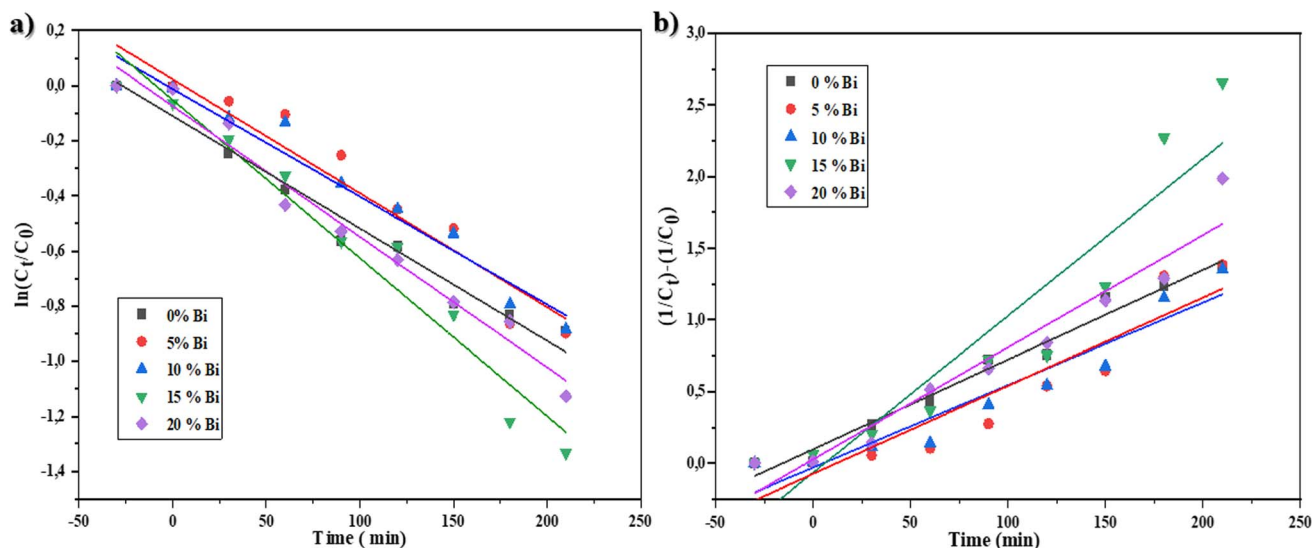
Fig. 10 Nonlinear fitting of (a) PFO and (b) PSO models for RhB degradation.

was conducted, and the data was analysed using the first- and second-order rate models, as indicated by eqn (1) and (2), respectively.

$$\ln \frac{C_0}{C_t} = k_1 t \tag{1}$$

$$\frac{1}{C_t} - \frac{1}{C_0} = k_2 t \tag{2}$$

where C_0 is the initial concentration of RhB dye solution, C_t is the concentration of Rhodamine B solution at time t, k_1 is the first-order rate kinetics, k_2 is the second-order rate kinetics, and t is the visible light exposure time. The obtained plots are presented in Fig. 10.

The rate constant values and regression correlation coefficient (R^2) of the kinetic curves are provided in Table 3. The validity of the rate constants was assessed based on the regression correlation coefficient (R^2) of the kinetic plots.[49–52] It was observed that the R^2 values for the first-order rates are greater than 0.9222, while the R^2 values for the second-order rates were smaller (0.8). Consequently, the photocatalytic degradation follows the first-order rate model for the BBO catalyst ranging from 5% to 20%-Bi. However, the R^2 values for 0%-Bi–BBO correspond to the second-order rate. This observation can be explained by the manner in which the recombination rate of e^-–h^+ occurs, with the rate following a first-order rate law when one electron is excited and recombined with h^+, and a second-

order rate law when multiple e^-–h^+ recombination occur simultaneously within a photocatalyst particle.[49–53]

To examine the durability and reusability of the Bi%–BBO nanoparticles, RhB degradation recycling tests were carried out under the same conditions. As illustrated in Fig. 9b, the degradation efficiency of Bi%–BBO exhibited no apparent decrease after three cycles, indicating the outstanding stability and reusability of the photocatalyst. According to the above-mentioned study, a degradation mechanism was proposed for RhB molecules. Fig. 11 illustrates the mechanism of the degradation of RhB in the presence of BBO, playing the role of a photocatalyst and absorbing a photon whose energy is higher than the energy of its gap band. This absorption leads to the generation of an electron–hole pair in the valence band (VB) and the conduction band (CB), respectively.[54] The interaction between a pair of electron holes and oxygen and water molecules leads to the formation of superoxide radical ions and hydroxyl radicals, which are extremely active species that target dye molecules and degrade them into non-toxic molecules such as water (H_2O), carbon dioxide (CO_2), and inorganic ions.[55] The possible mechanism can be summarized be the following reactions:
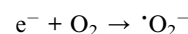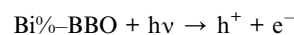
$$Bi\%\text{–}BBO + h\nu \rightarrow h^+ + e^-$$

$$e^- + O_2 \rightarrow {}^{\bullet}O_2{}^-$$

Table 3 Calculated parameters of kinetic order rate of RhB degradation on % Bi–BBO NPs

Bi% excess	First order		Second order	
	Rate constant ($k_1 \times 10^{-2}$ min^{-1})	R^2	Rate constant ($k_2 \times 10^{-2}$ min^{-1})	R^2
0% Bi–BBO	0.41	0.9674	0.6291	0.9787
5% Bi–BBO	0.41	0.9223	0.6149	0.8674
10% Bi–BBO	0.39	0.9569	0.5757	0.9123
15% Bi–BBO	0.57	0.9595	1.0951	0.8735
20% Bi–BBO	0.47	0.9762	0.7832	0.9416
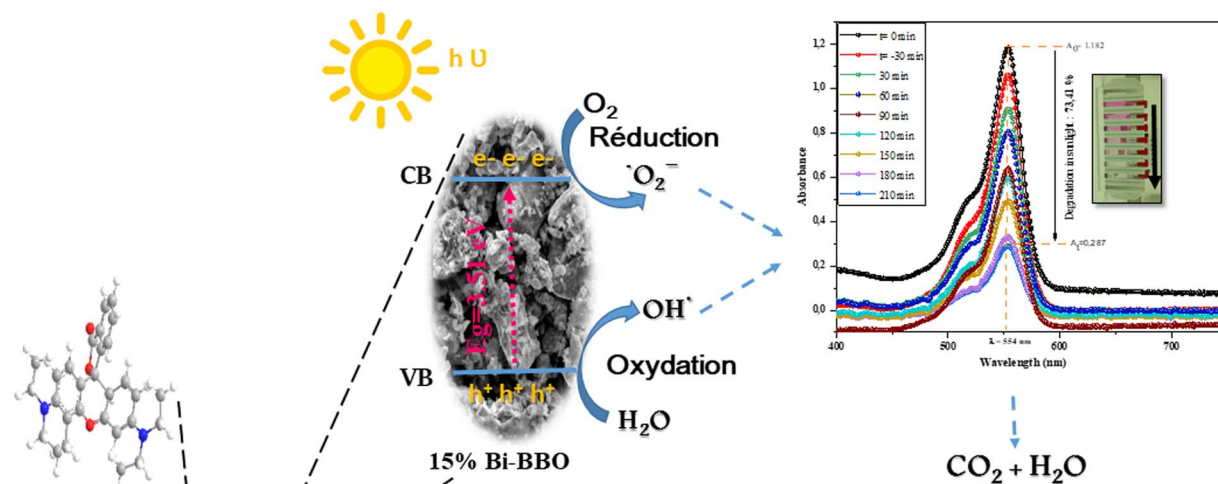
Fig. 11 Schematic illustration of basic mechanism.

$$\cdot O_2- + H^+ \rightarrow OH\cdot$$

$$RhB + \cdot O_2^-/OH\cdot \rightarrow CO_2 + H_2O + \text{inorganic ions}$$
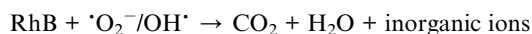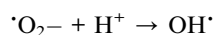
3.3. Antioxidant activity of Bi%–BBO

The DPPH method was effectively used to evaluate the antioxidant activity of the as-prepared % Bi–BBO NPs, which showed a change in color from violet to pale yellow (reduction). This reduction was examined by spectrophotometry at 517 nm. The DPPH radical scavenging activity varied as the concentration of BBO nanoparticles increased, as shown in Fig. 12a. Bi–BBO nanoparticles at

1 mg mL^{-1} concentrations of 0%, 5%, 10%, 15%, and 20% exhibited an inhibition percentage of 35.03%, 14.8%, 41.87%, 43.33%, and 29.45%, respectively. This percentage was 61.3%, 59.23%, 89.64%, 63.85%, and 60.66% at 5 mg mL^{-1}.

In addition to the observation of antioxidant activity by the nanoparticles, the antioxidant activity of ascorbic acid as a standard at 1 mg mL^{-1} was determined to be 45.47%, while at 5 mg mL^{-1} it was noted to be 96.42%. The results illustrate absolutely that the Bi%–BBO nanoparticles capture free radicals in a dose dependent manner. To evaluate the efficacy of the antioxidant activity, the IC50 value was calculated. The IC50 is the sample concentration required to capture 50% of the free
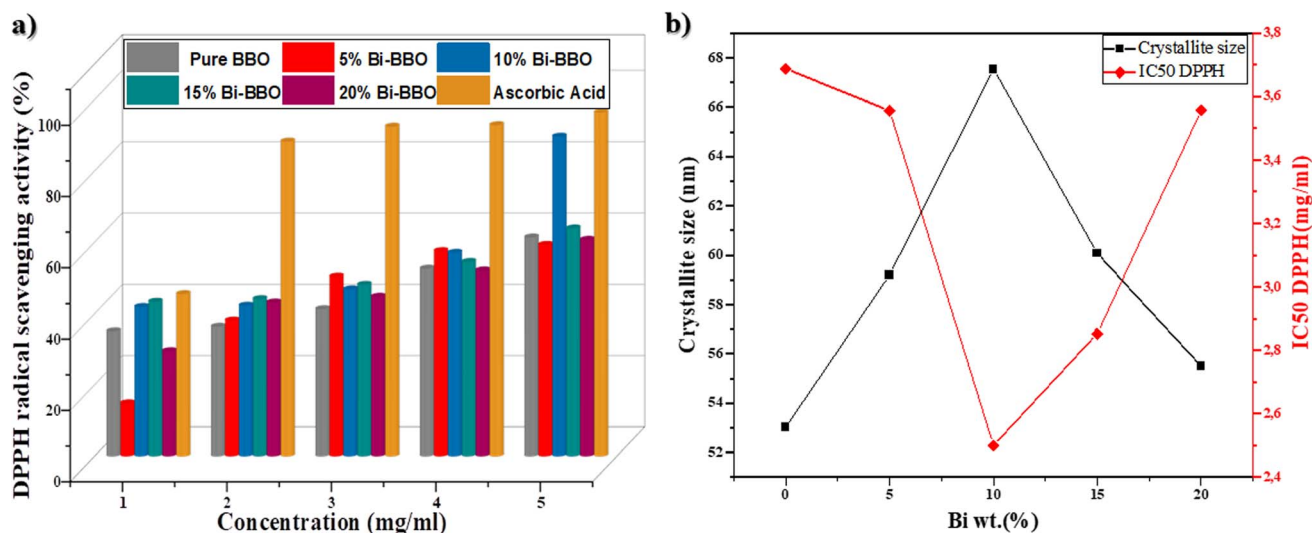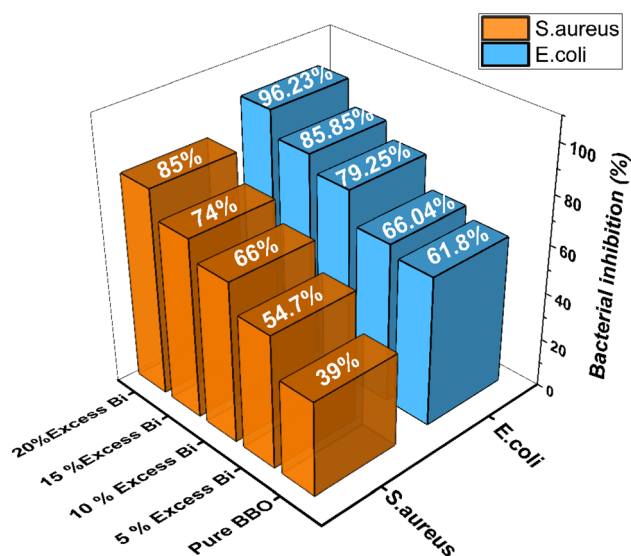

Fig. 12 (a) DPPH radical scavenging activity of % Bi–BBO and ascorbic acid. (b) Relationship between IC50 DPPH and crystallite size.

Table 4 Results of IC50 DPPH values for the different NPs and ascorbic acid

NPs	IC50 DPPH (mg mL^{-1})
Ascorbic acid	1.178
Pure BBO	3.688
05% Bi–BBO	3.556
10% Bi–BBO	2.500
15% Bi–BBO	2.853
20% Bi–BBO	3.557

Fig. 13 Bacterial inhibition (%) of pure BBO and BBO with different excess Bi (%) against *E. coli* and *S. aureus*.

radicals. The IC50 value decreases as the antioxidant capacity increases. The most effective (optimum) IC50 value was obtained for 10% Bi–BBO, with a concentration of 2.50 mg mL^{-1} (Table 4). The reason for this is possibly related to the size of the crystallites (67 nm), as mentioned in Fig. 12b.

3.4. Bi%–BBO as antibacterial agent

The 96-well plate microdilution method was used to test the antibacterial impact of the Bi%–BBO. The percentage of bacterial inhibition with pure BBO and BBO with various amounts of extra Bi (5%, 10%, 15%, and 20%) is shown in Fig. 13. The bacterial inhibition % against *S. aureus* (39%) and *E. coli* (61%) was demonstrated by pure BBO. *S. aureus* (96.23%) and *E. coli* (85%) were the two bacteria with the highest percentage of bacterial inhibition when Bi was present in excess of 20% (Fig. 12). The antibacterial activity of Bi%–BBO was found to be directly related to the excess % of Bi. The excess of Bi in the material is due to the fact that Bi substitutes Ba in increasing proportions, while the $Ba_{1-x}Bi_xBiO_3$ structure tends to become Bi_2O_3, which has excellent antibacterial activity according to the works of Liu *et al.*[56] with a percentage of bacterial inhibition of 92%.

At a Bi 20% surplus, the bacteria showed the strongest antibacterial action. Compared to the other microorganisms utilized in the experiment, Bi%–BBO (Bi 20%) demonstrated the strongest antibacterial activity against *S. aureus*. This may be explained by the absence of exterior lipids, which all Gram-positive bacteria possess and protect the cell wall, making them the most vulnerable in contrast to Gram-negative bacteria.[47]

4. Conclusion

Herein, a sol–gel process was used to prepare BaBiO$_3$ nanoparticles. The structural, morphological, and optical properties of the as-synthesized material were successively studied. The XRD analysis revealed the formation of a monoclinic structure of BaBiO$_3$ and the existence of a secondary BaCO$_3$ phase in all the Bi%–BBO samples (BaBiO$_3$–BaCO$_3$). 20% Bi–BBO exhibited a higher specific surface area than 0% Bi–BBO. Furthermore, the series of Bi%–BBO showed enhanced photocatalytic activity, where the highest degradation rate was exhibited by 15% Bi%–BBO (73%). The synthesized BBO exhibited antibacterial activity against Gram-positive and Gram-negative, where the highest antibacterial activity was found against *S. aureus* (96.23%). In addition, strong antioxidant effects were observed against the DPPH radical (89%). Therefore, the synthesis of BBO with differing excess of Bi resulted in the formation of a BBO–BCO binary composite. The successful application of BBO–BCO nanoparticles in the treatment of polluted water, as well as their efficacy for numerous medical applications have been proven.

Conflicts of interest

There are no conflicts to declare.

References

1 S. Larsson, M. Jansson and Å. Boholm, *J. Nanopart. Res.*, 2019, **21**, 1–17.

2 M. Nasrollahzadeh, M. Atarod, M. Sajjadi, S. M. Sajadi and Z. Issaabadi, *Interface Sci. Technol.*, 2019, **28**, 199–322.

3 M. Knell, *Nanotechnology and the Challenges of Equity, Equality and Development*, 2010, pp. 127–143.

4 S. Linic, U. Aslam, C. Boerigter and M. Morabito, *Nat. Mater.*, 2015, **146**, 567–576.

5 R. Darabi, F. E. D. Alown, A. Aygun, Q. Gu, F. Gulbagca, E. E. Altuner, H. Seckin, I. Meydan, G. Kaymak, F. Sen and H. Karimi-Maleh, *Int. J. Hydrogen Energy*, 2023, **48**, 21270–21284.

6 S. T. Khan, J. Musarrat and A. A. Al-Khedhairy, *Colloids Surf., B*, 2016, **146**, 70–83.

7 S. Kaushal, S. S. Nanda, S. Samal and D. K. Yi, *ChemBioChem*, 2020, **21**, 576–600.

8 M. T. Yaraki, S. Zahed Nasab, I. Zare, M. Dahri, M. Moein Sadeghi, M. Koohi and Y. N. Tan, *Ind. Eng. Chem. Res.*, 2022, **61**, 7547–7593.

9 A. Muthuvel, M. Jothibas and C. Manoharan, *Nanotechnol. Environ. Eng.*, 2020, **5**, 1–19.

10 A. Muthuvel, M. Jothibas and C. Manoharan, *J. Environ. Chem. Eng.*, 2020, **8**, 103705.

11 S. Zeghoud, H. Hemmami, B. Ben Seghir, I. Ben Amor, I. Kouadri, A. Rebiai, M. Messaoudi, S. Ahmed, P. Pohl and J. Simal-Gandara, *Mater. Today Commun.*, 2022, **33**, 104747.

12 H. Daneshvar, A. Tavakoli Kareshk, I. Sharifi, A. Keyhani, R. Tavakoli Oliaee and A. Asadi, *Iran. J. Parasitol.*, 2018, **13**, 515.

13 F. Ameen, A. Aygun, A. Seyrankaya, R. N. Elhouda Tiri, F. Gulbagca, İ. Kaynak, N. Majrashi, R. Orfali, E. N. Dragoi and F. Sen, *Environ. Res.*, 2023, **220**, 115231.

14 L. H. Mohammed, F. Gulbagca, R. N. E. Tiri, A. Aygun, M. Bekmezci and F. Sen, *Chem. Eng. J. Adv.*, 2023, **14**, 100495.

15 R. Darabi, H. Karimi-Maleh, S.-A. Shahidi, F. Gulbagca, R. Nour Elhouda Tiri, A. Monadi Sefidan, N. Dehdashtian, W. Alhrasishawi, A. Aygun, E. Esra Altuner and F. Sen, *Fuel*, 2023, **352**, 128841.

16 A. Aridi, D. Naoufal, H. El-Rassy and R. Awad, *Chem. Afr.*, 2023, 1–14.

17 A. L. Jadhav and S. M. Khetre, *Int. Nano Lett.*, 2020, **10**, 23–31.

18 R. Scholder, K. -W Ganter, H. Gläser and G. Merz, *Zeitschrift für anorganische und allgemeine Chemie*, 1963, **319**, 375–386.

19 K. V. Shilna, S. C. Sahoo and K. J. Thomas, *Appl. Mater. Today*, 2022, **27**, 101427.

20 C. Chaillout, A. Santoro, J. P. Remeika, A. S. Cooper, G. P. Espinosa and M. Marezio, *Solid State Commun.*, 1988, **65**, 1363–1369.

21 N. V. Barkovskii, *Russ. J. Gen. Chem.*, 2019, **892**, 173–184.

22 R. P. S. M. Lobo and F. Gervais, *Phys. Rev. B: Condens. Matter Mater. Phys.*, 1995, **52**, 13294.

23 A. S. Chouhan, E. Athresh, R. Ranjan, S. Raghavan and S. Avasthi, *Mater. Lett.*, 2018, **210**, 218–222.

24 D. E. Cox and A. W. Sleight, *Acta Crystallogr., Sect. B: Struct. Sci.*, 1979, **35**, 1–10.

25 R. P. S. M. Lobo and F. Gervais, *Solid State Commun.*, 1996, **98**, 61–63.

26 R. Bhargava, S. Khan, N. Ahmad and M. M. N. Ansari, *AIP Conf. Proc.*, 2018, **1953**, 030034.

27 M. B. Tahir, M. Sohaib, M. Sagir and M. Rafique, *Encyclopedia of Smart Materials*, 2022, 578.

28 Q. Guo, Y. Huang, H. Xu, D. Luo, F. Huang, L. Gu, Y. Wei, H. Zhao, L. Fan and J. Wu, *Solid State Sci.*, 2018, **78**, 95–106.

29 A. W. Sleight, *Phys. C*, 2015, **514**, 152–165.

30 J. Ge, W. J. Yin and Y. Yan, *Chem. Mater.*, 2018, **30**, 1017–1031.

31 J. Tang, Z. Zou and J. Ye, *J. Phys. Chem. C*, 2007, **111**, 12779–12785.

32 S. Jain, K. Sharma and U. Chandrawat, *Iran. J. Energy Environ.*, 2016, 7(1), 64–71.

33 K. Sharma, S. Jain and U. Chandrawat, *Iran. J. Energy Environ.*, 2016, **7**, 274–281.

34 J. Gao, W. Zeng, B. Tang, M. Zhong and Q. J. Liu, *Chem. Phys. Lett.*, 2020, **761**, 138054.

35 M. Khraisheh, A. Khazndar and M. A. Al-Ghouti, *Int. J. Energy Res.*, 2015, **39**, 1142–1152.

36 W. Jaidee, W. Maneerat, R. J. Andersen, B. O. Patrick, S. G. Pyne and S. Laphookhieo, *Fitoterapia*, 2018, **130**, 219–224.

37 F. Djani, M. Omari and A. Martínez-Arias, *J. Sol-Gel Sci. Technol.*, 2016, **78**, 1–10.

38 N. Hashemi, H. Q. Alijani, F. Mousazadeh, S. Rahi, S. Darijani, F. Sharifi, H. Khalili, S. Iravani, F. Borhani, N. Zafarnia and M. Khatami, *Bioprocess Biosyst. Eng.*, 2021, **44**, 1957–1964.

39 U. Holzwarth and N. Gibson, *Nat. Nanotechnol.*, 2011, **69**, 534.

40 H. Fodil and M. Omari, *J. Inorg. Organomet. Polym. Mater.*, 2017, **27**, 1473–1481.

41 M. S. Martín-González, J. García-Jaca, E. Morán and M. Á. Alario-Franco, *Phys. C*, 1998, **297**, 185–191.

42 V. N. Sonkusare, R. G. Chaudhary, G. S. Bhusari, A. R. Rai and H. D. Juneja, *Nano-Struct. Nano-Objects*, 2018, **13**, 121–131.

43 T. Shahid, M. Arfan, A. Zeb, T. Bibi and T. M. Khan, *Nanomater. Nanotechnol.*, 2018, **8**, DOI: 10.1177/1847980418761775.

44 F. Legesse, K. Sreenu, S. Kena and K. Legesse, *Sci., Technol. Arts Res. J.*, 2015, **4**, 80.

45 D. S. Shtarev, A. V. Shtareva, R. Kevorkyants, M. S. Molokeev and N. Serpone, *Photochem. Photobiol. Sci.*, 2021, **20**, 1147–1160.

46 T. T. Lee, C. Y. Huang, C. Y. Chang, I. K. Cheng, C. L. Hu, C. Te Lee and M. Fujimoto, *J. Mater. Res.*, 2012, **27**, 2495–2502.

47 R. Strobel, M. Maciejewski, S. E. Pratsinis and A. Baiker, *Thermochim. Acta*, 2006, **445**, 23–26.

48 S. Yurdakal, C. Garlisi, L. Özcan, M. Bellardita and G. Palmisano, *Heterogeneous Photocatalysis: Relationships with Heterogeneous Catalysis and Perspectives*, 2019, pp. 87–152.

49 P. C. Bhomick, A. Supong, S. Kumar, A. I. Sema, T. Merry and D. Sinha, *Water Conservation Science and Engineering*, 2023, **8**, 1–15.

50 J. Huang, A. R. Zimmerman, H. Chen and B. Gao, *Environ. Pollut.*, 2020, **258**, 113809.

51 A. I. Sema and J. Bhattacharyya, *J. Indian Chem. Soc.*, 2022, **99**, 100791.

52 B. Ohtani, *J. Photochem. Photobiol., C*, 2010, **11**, 157–178.

53 M. Madhukara Naik, H. S. Bhojya Naik, G. Nagaraju, M. Vinuth, K. Vinu and R. Viswanath, *Nano-Struct. Nano-Objects*, 2019, **19**, 100322.

54 V. Gupta and S. Singh, *Chemistry of Inorganic Materials*, 2023, **1**, 100008.

55 T. L. Yusuf, B. O. Orimolade, D. Masekela, B. Mamba and N. Mabuba, *RSC Adv.*, 2022, **12**, 26176–26191.

56 Q. Liu, J. Li, X. Zhong, Z. Dai, Z. Lu, H. Yang and R. Chen, *Adv. Powder Technol.*, 2018, **29**, 2082–2090.